

PAPER

Rarefied gas electro jet (RGEJ) micro-thruster for space propulsion

To cite this article: Ariel Blanco and Subrata Roy 2017 *J. Phys. D: Appl. Phys.* **50** 455201

View the [article online](#) for updates and enhancements.

Rarefied gas electro jet (RGEJ) micro-thruster for space propulsion

Ariel Blanco and Subrata Roy 

Applied Physics Research Group, Mechanical and Aerospace Engineering Department, University of Florida, Gainesville, FL 32611, United States of America

E-mail: roy@ufl.edu

Received 21 July 2017, revised 11 September 2017

Accepted for publication 13 September 2017

Published 13 October 2017



CrossMark

Abstract

This article numerically investigates a micro-thruster for small satellites which utilizes plasma actuators to heat and accelerate the flow in a micro-channel with rarefied gas in the slip flow regime. The inlet plenum condition is considered at 1 Torr with flow discharging to near vacuum conditions (<0.05 Torr). The Knudsen numbers at the inlet and exit planes are ~ 0.01 and ~ 0.1 , respectively. Although several studies have been performed in micro-hollow cathode discharges at constant pressure, to our knowledge, an integrated study of the glow discharge physics and resulting fluid flow of a plasma thruster under these low pressure and low Knudsen number conditions is yet to be reported. Numerical simulations of the charge distribution due to gas ionization processes and the resulting rarefied gas flow are performed using an in-house code. The mass flow rate, thrust, specific impulse, power consumption and the thrust effectiveness of the thruster are predicted based on these results. The ionized gas is modelled using local mean energy approximation. An electrically induced body force and a thermal heating source are calculated based on the space separated charge distribution and the ion Joule heating, respectively. The rarefied gas flow with these electric force and heating source is modelled using density-based compressible flow equations with slip flow boundary conditions. The results show that a significant improvement of specific impulse can be achieved over highly optimized cold gas thrusters using the same propellant.

Keywords: micro thruster, mixed numerical formulation, multispecies plasma model, rarified gas dynamics, plasma discharge, localized heating, high altitude application

(Some figures may appear in colour only in the online journal)

1. Introduction

The use of small satellites has gained interest in recent years due to their smaller overall life cycle cost [1]. Micro-propulsion systems for small satellites face several issues: contamination, passage clogging, less reliability, less durability, and excessive complexity. Micro-thrusters must produce minimum impulse bits, $O(\mu\text{Ns})$, determined by attitude control requirements [1]. In contrast, the thrust requirements for slew manoeuvres extends into the $O(\text{mN})$ range, very large when compared to the impulse bits requirements. Micro-propulsion systems must overcome these issues while being lightweight, compact, low power, efficient, and inexpensive. Cold gas thrusters (CGT) have desirable advantages for micro-propulsion applications [1]. However, valve leakage or low specific impulse (I_{sp}) for

desirable propellants, eliminate CGT from consideration for primary propulsion tasks unless the required $\Delta - v$ is small ($<100 \text{ m s}^{-1}$) [1]. Their I_{sp} is typically low unless very light gases are used (e.g. H_2 or He), which produce experimentally measurable specific impulses of 272 and 165 (s), respectively [1]. Very light gases are commonly not used due to storage problems. For argon propellant, the I_{sp} of a highly optimized CGT is 52 (s) [1].

In order to increase the I_{sp} of CGT, the free molecule micro-resistojet (FMMR) was proposed [1]. FMMR operates at low stagnation pressures (50–500 Pa) and large exit Knudsen numbers ($\text{Kn} \sim 1$) [1]. Due to the low pressures, gas heating occurs primarily by conduction [2]. FMMR operating with a heating element temperature of 600 K can produce an I_{sp} of 68 (s) for water and 45 (s) for argon propellant [1]. These

values may not look like an improvement, but due to the low stagnation pressure, liquid propellant could be vaporized on demand, thus avoiding heavy storage tanks and valve leakage [1]. Unfortunately, FMMR suffers from significant thermal energy losses due to thermal dissipation [3]. An estimate by Micci and Ketsdever [1] predicts a heat loss of 6800 (mW) for a device operating with 40 expansion slots that requires 6000–8000 (mW) to heat the propellant gas [1]. The proposed rarefied gas electro jet (RGEJ [4]) micro-thruster aims to improve the heat loss of microelectromechanical (MEMS) based microresistojet thruster designs.

Other designs improving the I_{sp} of CGT using plasma aided technologies are the micro-plasma thruster (MPT [5]), the radio-frequency electrothermal thruster (RFET [6]), and the microwave electrothermal thruster (MET [7]). The MPT consists of a cylindrical geometry comprising a constant area section, 500 μm long and 100 μm in diameter, and a diverging nozzle. The MPT uses a direct-current micro-discharge in the abnormal glow regime. It operates with argon at a stagnation pressure of 100 (Torr), two orders of magnitude higher than the RGEJ, in the slip flow regime with $\text{Kn} \sim 0.01$ at the inlet and $\text{Kn} \sim 0.08$ at the exit plane [8]. In the MPT, the expansion and heating of the flow occur predominantly in the diverging nozzle. The thrust difference between no-slip and slip boundary condition cases is 2–3% since the majority of the thruster, the constant area section, experiences low Kn numbers ($0.01 < \text{Kn} < 0.03$) [8]. Due to a small volume-to-surface (V/S) ratio (39.2 μm) the thermal losses, caused by conduction to the walls, are expected to be significant. For comparison, the RGEJ has a V/S ratio of 1.5 (mm) and operates in the slip flow regime with $\text{Kn} \sim 0.01$ at the inlet and $\text{Kn} \sim 0.1$ at the exit plane with more than 50% of the device experiencing ($\text{Kn} > 0.05$). Using no-slip boundary conditions would produce a drastically different solution in the RGEJ. The MPT's I_{sp} is 74 (s) for the 750 (V) and 650 (mW) case, an improvement over CGT by a factor of (~ 1.5) [8]. However, the MPT's thrust effectiveness, the difference in thrust with and without plasma heating divided by the total electrical power, is very low (50 $\mu\text{N W}^{-1}$) due to thermal losses through the isothermal walls [5, 8].

The RFET consist of a cylindrical geometry, 18 mm in length and 4.2 mm in diameter, composed of alumina with copper electrodes operating at a frequency of 13.56 MHz and an electric potential difference of 240 V. For an argon gas plenum pressure of 1.5 (Torr), the power consumption is 10 W, causing an ionization degree of 0.44% and a maximum electron number density of 2×10^{18} (m^{-3}) [6]. The predicted mass flow rate and thrust are 100 SCCM and 2.619 mN [9]. The MET has a cylindrical dielectric chamber, 10 mm long and 1.5 mm in diameter, with a metal rod antenna on the axis to produce microwave signals at 4 GHz that generate the plasma and heat the gas. The heated argon gas in the chamber at high pressure (10–50 kPa) is expanded through a Laval nozzle. An experiment performed with 31 kPa plenum pressure produced a 60 SCCM mass flow rate and a 1.4 (mN) thrust. Both of these thrusters operate with higher power consumption than the target power budget of RGEJ (< 5 W), but they produce higher specific impulse ($I_{sp} > 80$ s) than the RGEJ and the MPT. These designs help illustrate the many

different examples of plasma aided technology thrusters currently under investigation.

The RGEJ design aims to increase the efficiency of the energy exchange from the electrical source to the propellant. It operates in the slip flow regime, which decreases viscous losses and heat transfer to the walls. The RGEJ concept involves localized embedding of electrodes with either a DC or an RF applied potential difference, along the dielectric walls to produce a glow discharge plasma [3]. The charged particles in the plasma are accelerated by the electric field, heating the propellant. The presence of charged particles implies that both electric and magnetic fields could be used to produce thrust. In this study, magnetic fields are not used and the thruster operates with a DC discharge. A finite element and a finite difference based numerical analysis of the rarefied gas and the ionized gas are implemented, respectively, to model the RGEJ. The cases presented, display a non-optimized design with adiabatic walls and a low plenum pressure (1 Torr), operating at different DC voltages. It is important to emphasize that adiabatic walls, instead of isothermal, requires a more robust iterative procedure between the loosely coupled code modules.

2. Methodology

In order to simulate the RGEJ, an existing, previously described in literature, in-house modular multi-scale ionized gas (MIG) flow solver platform developed by Balagangadhar and Roy [10, 11] was used. The MIG code consists of two modules: a finite element based rarefied gas module (RGM) and a finite difference based ionized gas module (IGM), which was recently developed. They are loosely coupled in the following sequence. The RGM runs until convergence, producing the gas density (ρ), components of velocity (u , v), and temperature (T). These variables from the RGM are passed to the IGM. Then, the IGM runs until convergence, producing the plasma induced electrostatic force components (F_x , F_y) and the electro-thermal heating source (Q) needed by the new run of the RGM. The information obtained by each module is exchanged in this fashion until the steady-state solution is obtained. The following figure shows the process.

In figure 1, the first step initializes the variables of both modules, including the initial voltage (V_i) value, based on the plasma breakdown voltage of the gas (~ 150 V for argon). Each module uses the L^2 -norm of the solution to test for convergence. After both modules have reached convergence at a given voltage, the voltage is increased by a voltage difference (ΔV) and the process is repeated, until the maximum voltage (V_{max}) desired is achieved. For all cases in this study, (ΔV) is 50 V. After reaching the maximum voltage (V_{max}), a test for global convergence is performed. The RGM and the IGM are run for 5 time steps even if their L^2 -norms are less than their tolerances. If the L^2 -norm of each module is less than its tolerance for all five consecutive time steps for three consecutive iterative loops between the RGM and the IGM, then global convergence conditions are satisfied. The L^2 -norms for the RGM and the IGM, using the given non-dimensionalization explained in the following sections, are 10^{-4} and

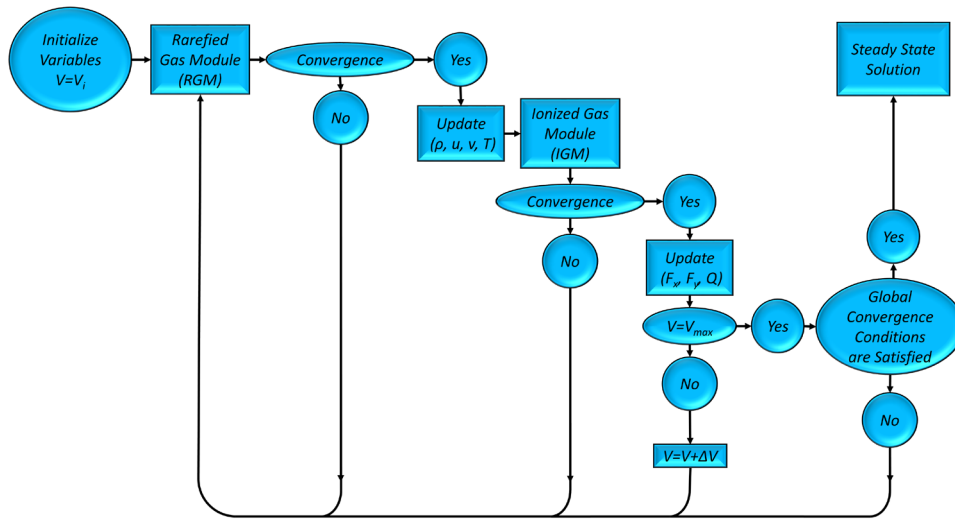


Figure 1. Schematic of the new MIG code with rarefied gas and IGMs.

10^{-10} for time steps of 10^{-8} and 5×10^{-13} s for each module, respectively.

2.1. Ionized gas module (IGM)

2.1.1. Plasma governing equations and argon chemistry. The numerical model for the argon plasma assumes a weakly ionized gas composed of positive ions, three types of metastable atoms, and electrons. In fluid models of glow discharges, all plasma species are treated as a continuum. Momentum equations are usually reduced to the drift-diffusion equation. In the local mean energy approximation (LMEA) model, the spatial distribution of the electron temperature is obtained from the solution of the energy balance equation for electrons [12]. The calculation of the electron transport coefficients (mobility and diffusion) and the kinetic coefficients (electron-impact reaction rates for excitation and ionization processes) are done by solving the kinetic Boltzmann equation as functions of the electron energy [12]. The continuity equation that is solved for each plasma species is given as [13]

$$\frac{\partial n_k}{\partial t} + \nabla \cdot \Gamma_k = S_k, \text{ where } \Gamma_k = \text{sgn}(q_k)\mu_k n_k \mathbf{E} - D_k \nabla n_k + n_k \mathbf{V}. \quad (1)$$

The right-hand side of equation (1) contains the source and sink terms representing the argon chemistry, similar in notation to Rafatov *et al* [14]. The subscript k is equal to: i , e , S-levels, P-levels, or D-levels, for ions, electrons, and three types of metastable atoms, respectively. \mathbf{V} is the velocity vector of the bulk gas obtained from the rarefied gas module [15]. The electron energy equation is included in LMEA in order to incorporate the nonlocal transport of electrons written as recommended by Hagelaar and Pitchford [16]

$$\frac{\partial n_\epsilon}{\partial t} + \nabla \cdot \Gamma_\epsilon = -e\Gamma_e \cdot \mathbf{E} - \frac{3}{2}n_e \frac{2m_e}{m_g} \nu_{ea} k_b (T_e - T_g) - e \sum_j \Delta E_j^e r_j, \quad (2)$$

where $\Gamma_\epsilon = -\mu_\epsilon n_\epsilon \mathbf{E} - D_\epsilon \nabla n_\epsilon + \frac{5}{3}n_\epsilon \mathbf{V}$.

The first term on the right-hand-side of equation (2) describes the Joule heating, which is responsible for adding energy to

electrons. The second and third term describe the electron energy losses due to the inelastic and elastic collisional processes [17]. The notation has been previously explained by Rafatov *et al* [12]. The elementary reactions considered for low-pressure, argon chemistry are given in table 1.

The cross-sections for these reactions were obtained from [18] and the *kinetic model section* of Petrov and Ferreira [19]. Detailed balancing was used for the reverse reaction of all ‘excitation’ and ‘transition between excited states’ reactions. The electron transport coefficients (μ_e and D_e) are calculated using an electron Boltzmann equation solver, Bolsig+ [16], as functions of the mean electron energy (ϵ) and the energy transport coefficients are related to the particle transport coefficients via $\mu_\epsilon = (5/3)\mu_e$ and $D_\epsilon = (5/3)D_e$. The ion mobility and diffusion coefficients are obtained from equation (17) in Rafatov *et al* [20], and Einstein relation, ($D_i = k_b T_i \mu_i / e$), respectively. The metastable mobility is zero for all the metastable species in this model and the metastable diffusion is the same as in Deconinck [8]. All heavy, metastable and ion species are assumed to be in thermal equilibrium with the gas. The volume source terms (S_k) in equation (1) are determined by the reactions occurring within the discharge, where the source terms (S_i , S_e) for ions and electrons are identical due to particle conservation. The neutral species number density (n_n) is solved using the ideal gas law.

The system of equations is closed with the solution of the electrostatic Poisson equation in order to calculate the electric field (12)

$$\epsilon_0 \nabla \cdot \mathbf{E} = \sum_k q_k n_k, \text{ where } \mathbf{E} = -\nabla \phi. \quad (3)$$

The governing equations are written in the non-dimensional form using reference number density of 10^{16} (m^{-3}), an electric potential of 100 (V), a length scale of 0.01 (m), an electron temperature of 10 (eV) and a time scale of 10^{-10} (s).

2.1.2. Plasma electrostatic force and electro-thermal heating source. The plasma induced electrostatic force and plasma electro-thermal heating source are calculated as [8, 21]

Table 1. Relevant reactions. All rates calculated using Bolsig+ unless otherwise stated [16].

Index	Reaction	Type	ΔE_f^e (eV)	Coefficient
1	$e + \text{Ar} \rightarrow e + \text{Ar}$	Elastic collision	0	Boltz. [18]
2	$e + \text{Ar} \rightarrow 2e + \text{Ar}^+$	Direct ionization	15.7	Boltz. [18]
3	$e + \text{Ar} \leftrightarrow e + \text{Ar}_{(S\text{-Levels})}^*$	Excitation	11.55	Boltz. [18]
4	$e + \text{Ar} \leftrightarrow e + \text{Ar}_{(P\text{-Levels})}^*$	Excitation	13.0	Boltz. [18]
5	$e + \text{Ar} \leftrightarrow e + \text{Ar}_{(D\text{-Levels})}^*$	Excitation	14.0	Boltz. [18]
6	$e + \text{Ar}_{(S\text{-Levels})}^* \rightarrow 2e + \text{Ar}^+$	Stepwise ionization	4.07	Boltz. [19]
7	$e + \text{Ar}_{(P\text{-Levels})}^* \rightarrow 2e + \text{Ar}^+$	Stepwise ionization	2.52	Boltz. [19]
8	$e + \text{Ar}_{(D\text{-Levels})}^* \rightarrow 2e + \text{Ar}^+$	Stepwise ionization	1.66	Boltz. [19]
9	$e + \text{Ar}_{(S\text{-Levels})}^* \leftrightarrow e + \text{Ar}_{(P\text{-Levels})}^*$	Trans. b/w excited states	1.51	Boltz. [19]
10	$e + \text{Ar}_{(P\text{-Levels})}^* \leftrightarrow e + \text{Ar}_{(D\text{-Levels})}^*$	Trans. b/w excited states	0.90	Boltz. [19]
11	$\text{Ar}_{(S\text{-Levels})}^* + \text{Ar}_{(S\text{-Levels})}^* \rightarrow \text{Ar}^+ + \text{Ar} + e$	Penning ionization	—	$5.0 \times 10^{-16} \text{ m}^3 \text{ s}^{-1}$ [19]
12	$\text{Ar}_{(P\text{-Levels})}^* + \text{Ar}_{(P\text{-Levels})}^* \rightarrow \text{Ar}^+ + \text{Ar} + e$	Penning ionization	—	$5.0 \times 10^{-16} \text{ m}^3 \text{ s}^{-1}$ [19]
13	$\text{Ar}_{(P\text{-Levels})}^* + \text{Ar}_{(S\text{-Levels})}^* \rightarrow \text{Ar}^+ + \text{Ar} + e$	Penning ionization	—	$5.0 \times 10^{-16} \text{ m}^3 \text{ s}^{-1}$ [19]
14	$\text{Ar}_{(P\text{-Levels})}^* + 2\text{Ar} \rightarrow \text{Ar}_{(S\text{-Levels})}^* + 2\text{Ar}$	Trans. b/w excited states	—	$5.0 \times 10^{-44} \text{ m}^6 \text{ s}^{-1}$ [19]
15	$\text{Ar}_{(P\text{-Levels})}^* + \text{Ar} \rightarrow \text{Ar}_{(S\text{-Levels})}^* + \text{Ar}$	Trans. b/w excited states	—	$5.0 \times 10^{-17} \text{ m}^3 \text{ s}^{-1}$ [19]
16	$\text{Ar}_{(S\text{-Levels})}^* \rightarrow \text{Ar} + h\nu$	Radiation	—	$7.0 \times 10^8 \text{ 1 s}^{-1}$ [19]
17	$\text{Ar}_{(D\text{-Levels})}^* \rightarrow \text{Ar} + h\nu$	Radiation	—	$5.96 \times 10^8 \text{ 1 s}^{-1}$ [19]
18	$\text{Ar}_{(P\text{-Levels})}^* \rightarrow \text{Ar}_{(S\text{-Levels})}^* + h\nu$	Radiation	—	$3.76 \times 10^8 \text{ 1 s}^{-1}$ [19]
19	$\text{Ar}_{(D\text{-Levels})}^* \rightarrow \text{Ar}_{(P\text{-Levels})}^* + h\nu$	Radiation	—	$1.46 \times 10^8 \text{ 1 s}^{-1}$ [19]

$$\mathbf{F} = e (n_i - n_e) \mathbf{E}, \quad (4)$$

$$\mathbf{Q} = e (\Gamma_i \cdot \mathbf{E}), \quad (5)$$

where the subscripts i and e were previously defined in equation (1).

In equation (5), the term on the RHS is the ion Joule heating, since only the heavy particles thermalize with the bulk gas. The ion Joule heating term usually has a thermalization factor that accounts for the fraction of energy that is locally equilibrated with the gas. In a xenon discharge at 100 (Torr), it was assumed by Boeuf *et al* [22] that only 25% of the energy was deposited in the neutral gas and the maximum gas temperature (~460 K) of their simulation matched relatively well with the gas temperature (~500 K) obtained from experiments. In this case, the ion Joule heating rapidly equilibrates with the gas since the ion-neutral mean free path is orders of magnitude smaller than the device length scale, a conservative approach is taken to obtain the upper bound for the gas heating, and the thermalization factor is assumed to be equal to one [21].

2.1.3. Plasma boundary conditions. The boundary conditions for ions, electrons, metastable atoms, and electron energy density at the anode, cathode, and dielectric surfaces (walls) are the same as in Rafatov *et al* [12], where the secondary electron emission coefficient (γ) is picked to have a value of 0.07 [23]. For the electric potential boundary conditions, (ϕ) is equal to the zero at the anode and the negative value of the discharge voltage at the cathode, while at the dielectric surface, the surface charge equation is used as in Rafatov *et al* [12]. The charged or metastable species impacting the surface are assumed to recombine instantly at the solid walls. Symmetry condition is imposed at the bottom of the channel since only half of the domain is simulated, and zero particle flux

is imposed for the inlet: $\Gamma_{x,k} = 0$, $\Gamma_{x,\epsilon} = 0$, $\partial\phi/\partial x|_{x=0} = 0$ for numerical stability reasons. The inlet boundary is sufficiently far away from the cathode region and has no influence on the plasma output parameters: \mathbf{F} and \mathbf{Q} [8]. In an open face boundary, the particles are assumed to flow out of the domain with the velocity of the bulk gas, flux conditions are imposed for all particles, and homogeneous Neumann condition is used for the electric potential. Open face is imposed for the exit plane: $\Gamma_{x,k} = n_k V_x$, $\Gamma_{x,\epsilon} = (5/3) n_e V_x$, $\partial\phi/\partial x|_{x=L} = 0$.

2.1.4. IGM numerical methodology. The system of governing equations for the plasma is solved using the semi-implicit, finite difference scheme module of the multiscale ionized gas (MIG) code [10, 11]. The equations are solved decoupled starting with the steady Poisson equation, then the ion continuity equation, and the three metastable atoms continuity equations. The electron continuity and electron energy density equations are solved coupled with each other. Poisson equation is approximated by combining the continuity equations of ions and electrons to predict the charge at present time step as

$$\nabla^2 \phi^{n+1} = -\frac{e}{\epsilon_0} (n_i^{n+1} - n_e^{n+1}) \approx -\frac{e}{\epsilon_0} [n_i^n - n_e^n + \Delta t (\nabla \cdot \Gamma_e^n - \nabla \cdot \Gamma_i^n)]. \quad (6)$$

The Poisson equation is solved using second order central difference scheme where the right-hand-side is treated as a source since it depends on previous time step information. The continuity equations for ions, electrons, and metastable atoms are solved using central difference on a staggered mesh, where the face fluxes are discretized using the first order accurate Scharfetter–Gummel scheme [24] and the volume source terms (S_k) are treated explicitly. The time discretization is first order implicit Euler method, beneficial for stability purposes. The k subscript refers to ions, electrons, or metastable atoms ($k = i, e, S\text{-levels}, P\text{-levels}, D\text{-levels}$), n to the time-step, and

j to the node number. The electron energy density is solved in a similar manner, simultaneously with the electron continuity equation using a Newton–Raphson non-linear solver.

Each equation imposes a different restriction on the time step. The electric potential is updated based on the Maxwell time [17], while the heavy species fluxes restriction depends on the Courant–Friedrichs–Lewy (CFL) condition. The time step restrictions imposed by the electrons and the argon chemistry are stricter than the heavy species transport restrictions. The electron and the chemical source terms time step restrictions depend on the CFL condition imposed by the electron energy transport. In all our simulations, all of the equations are advanced at the most restrictive time step value from uniform initial conditions.

2.2. Rarefied gas module (RGM)

2.2.1. Rarefied gas governing equations. In the rarefied gas simulation, density-based compressible flow equations were used with the assumption of ideal gas using argon as the working fluid [25]. The continuity, momentum, and energy equations are given by equations (2)–(5) in Raju [25], with the additions of the terms (F_x , F_y , Q) in the right-hand-side of equations (3)–(5) in Raju [25], respectively. The ideal gas constant (R) and the specific heat at constant pressure (c_p) are considered constants, while the thermal conductivity (κ) and the viscosity (μ) are functions of the gas temperature [26]

$$\begin{aligned} \mu &= -4.688\,268 \times 10^{-18}T^4 + 2.608\,773 \times 10^{-14}T^3 - 5.761\,201 \times 10^{-11}T^2 + 9.224\,244 \times 10^{-8}T - 3.936\,359 \times 10^{-7}, \\ \kappa &= -3.591\,506 \times 10^{-15}T^4 + 2.006\,139 \times 10^{-11}T^3 - 4.456\,168 \times 10^{-8}T^2 + 7.199\,751 \times 10^{-5}T - 3.170\,661 \times 10^{-4}, \end{aligned}$$

where μ is in (Pa · s), κ is in ($\frac{W}{mK}$), and $[80\,(K) \leq T \leq 2000\,(K)]$. (7)

The governing equations are written in the non-dimensional form using a velocity of 100 (m s⁻¹), a length scale of 0.01 (m), a pressure of 100 (Pa), a temperature of 300 K, and density from the ideal gas law.

2.2.2. Slip flow boundary conditions. The Knudsen number (Kn) and mean free path (λ) are defined as [27, 28]

$$\text{Kn} = \frac{\lambda}{H} \text{ and } \lambda = \frac{1}{\sqrt{2}n\pi d^2} \cong \frac{16\mu}{5\rho} \sqrt{2\pi RT}, \quad (8)$$

where d , n and H , are the atomic diameter, gas number density, and channel height, which is much smaller than the channel length. Kn is used to determine which numerical modelling approach is more appropriate: statistical mechanics or continuum mechanics. As $\text{Kn} > 0$, the flow is assumed sufficiently continuous, while for $\text{Kn} > 10$, the flow is assumed free-molecule. For $10^{-3} < \text{Kn} < 10$ the flow is neither sufficiently continuum nor completely molecular [25]. For this range, the flow is further divided into two subcategories: slip flow regime $10^{-3} < \text{Kn} < 10^{-1}$ and transitional regime for $10^{-1} < \text{Kn} < 10$ as explained by Raju [25]. In our cases, Kn is in the slip regime by design.

The boundary conditions for the rarefied gas simulation are fixed stagnation density and temperature at the inlet ($\rho_0 = P_0/RT_0$, $T_0 = 300\text{ K}$, where $P_0 = 133.3\text{ Pa}$). Isentropic flow assumption is used to calculate the static density and temperature at the inlet plane. At the walls there is no penetration, the normal velocity is equal to zero. At the outlet, static pressure is assumed to be ($P_{\text{Out}} = 0.05\text{ Torr}$) if Mach number is subsonic and ($\rho_{\text{Out}} = P_{\text{Out}}/RT_{\text{Out}}$), else ρ is extrapolated from internal nodes. Boundary conditions for a rarefied gas are used for tangential velocity and temperature at the wall face, as described by Maxwell [29] and Smoluchowski [30], similar to Raju [25]. For example, for the top wall face inside the channel, the tangential velocity boundary condition is

$$-\frac{\mu}{\rho} \left(\frac{\partial u}{\partial y} \right) \Big|_{y=H/2} = \frac{5\sqrt{2\pi RT}}{16} \frac{\sigma_v}{(2 - \sigma_v)} \left[u - \frac{3}{4} \frac{\mu}{\rho T} \left(\frac{\partial T}{\partial x} \right) \Big|_{y=H/2} \right]. \quad (9)$$

If a case is adiabatic, $\partial T/\partial x = 0$ or $\partial T/\partial y = 0$ is used as a temperature boundary condition at the wall. The tangential momentum accommodation coefficient ($\sigma_v = 0.89$ [31]) and the thermal accommodation coefficient ($\sigma_T = 0.87$ [32]) found in the formulas of slip flow boundary conditions are selected based on average values for argon interacting with different materials. The rest of the boundary conditions needed are

zero flux normal to the edges of the domain [$\partial(\dots)/\partial x = 0$ or $\partial(\dots)/\partial y = 0$].

2.2.3. RGM numerical methodology. The plasma numerical simulation is performed using the IGM described in section 2.1 using equations (1)–(3), while the rarefied gas numerical simulation is performed using the rarefied gas module described in section 2.2.1. The rarefied gas simulations are modelled using finite element methods and loosely coupled with the IGM as shown in figure 1. The numerical simulation of the rarefied gas code is performed using an existing, finite element based module in the MIG [10, 11]. This module of MIG utilizes the Galerkin weak statement combined with the Newton–Raphson nonlinear solver. Bilinear elements are used in the RGC module for the numerical analysis of the RGEJ thruster. In order to provide stability to the solution, the inconsistent streamline up-winding (SU) artificial diffusion method in 2D is used [33]. The MIG flow solver platform had been utilized for many different applications, including electric propulsion, micro-flows, nanoscale flows, fluid dynamics, and plasma physics [34–37]. Most recently, the finite difference IGM has been added to extend MIG’s capabilities.

2.3. Geometry and grid

The micro-thruster was designed with a long (20 mm), narrow (3 mm) slot to prevent the possibility of catastrophically plugging the thruster's throat. The absence of an expansion nozzle at the exit of the channel is due to predicted low Reynolds numbers (<100). In the limit of continuum isentropic flow through a large pressure drop, the nozzle's thrust is proportional to the operating pressure and the throat area [1], where W and H are width and height,

$$F_{\text{Thrust}} \propto P_0 A_t \propto P_0 W H. \quad (10)$$

The Reynolds number gives a measure of nozzle efficiency in terms of viscous flow losses. The nozzle's Reynolds number at the throat is given by [1]

$$\text{Re} = \frac{\rho a H}{\mu} \propto \frac{P_0 H}{T_0^\beta}, \text{ where } (1.2 < \beta < 1.5) \text{ and } a = \sqrt{\gamma R T}. \quad (11)$$

For the nozzle's viscous losses to scale favourably, the Reynolds number must remain constant or increase as the device is miniaturized [1]. Since microsatellites require lower thrust and cannot operate at high enough plenum pressures, the operational Reynolds number for micro-nozzles may decrease to values as low as 100, and as heat is added, the flow experiences a further decrease in Reynolds number. Micro-thrusters with low throat Reynolds number (~ 100) do not experience any gains from an expansion nozzle [38]. The low plenum-pressure operation condition is chosen to scale the thrust and for the additional benefit of reduced propellant storage pressure, therefore easing the propellant tank mass and valve leakage requirements [1].

Figure 2 shows the domain region numerically simulated (light blue). The IGM module models only the region inside the channel, ($0 \text{ mm} < x < 20 \text{ mm}$), since the charged particle number densities are negligible at the exit plane. The mesh inside the channel has 401×31 nodes. For the cases tested, the anode is between ($1 \text{ mm} < x < 2 \text{ mm}$) and the cathode ($8 \text{ mm} < x < 19 \text{ mm}$). The RGM module models the channel region and the plume. The plume has 201×201 nodes and is 10×10 (mm). All cells are rectangular and have constant Δx and Δy . It is only necessary to solve one-half of the domain due to symmetry.

3. Results and discussion

3.1. Rarefied gas module benchmarking

In this section, a benchmarking of the rarefied gas module is done for subsonic gas flows through a micro-channels using results from Chen *et al* [39], which were validated within 1.15% accuracy with experimental results of Pong *et al* [40]. The model assumes the gas flows through two parallel plates of length L and width W separated by a distance H . The end effects are neglected and only the 2D geometry stretching in the x and y directions is considered.

In table 2 T_{in} is the inlet gas temperature and T_w is the isothermal wall temperature. $P_{\text{in}}/P_{\text{out}}$ is the ratio of inlet pressure versus outlet pressure, all other parameters and boundary

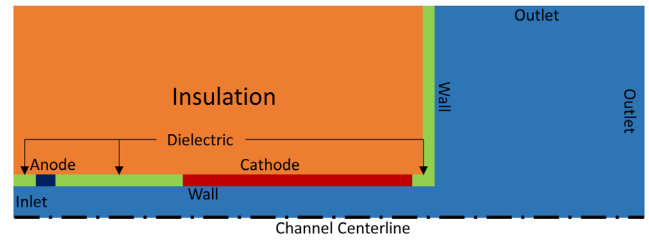


Figure 2. Geometry and design of cases tested.

conditions are given by Chen *et al* [39]. The inlet and outlet pressures produce Knudsen numbers of 0.0217 and 0.0585, respectively. The flow in the microchannel is in the slip flow regime, which is the regime of interest for this study.

The maximum discrepancy between Chen *et al* [39], see table 3, and our results, see table 4, in the u -velocity at the centreline, occurs at $x = 2500$ (μm). This maximum discrepancy of 1.6% can be attributed to using different values of thermal conductivity and different numerical schemes. Chen *et al* [39] did not provide the thermal conductivity and explicit finite difference method was used to solve the governing equations. The pressure discrepancy along the centreline is similar to the u -velocity discrepancy. Exact values for the pressure along the centreline are not given in Chen *et al* [39], only a figure is provided, therefore an exact comparison of the pressure is not performed. The temperature remains near constant throughout the domain ($\sim T_w = 314 \text{ K}$), and the v -velocity is close to zero. Overall, the rarefied gas module matched closely with results in literature.

3.2. Plasma module validation

In order to validate the plasma code, the veracity of the model was tested using the method of manufactured solutions with the same procedure as Houba [41]. Additionally, a simulation in 1D of a parallel-plate, capacitively coupled, low-pressure, symmetric RF discharge driven at 13.56 MHz was performed and compared with Godyak *et al* [42]. Although the RGEJ cases in this study use a DC applied potential difference, the RF discharge experiment of Godyak *et al* [42] is employed for this validation since the numerical models used for RF and DC glow discharges are almost identical except for the applied alternating voltage in RF discharges. In previous studies, Sitaraman and Raja [21] and Deconinck [8] have successfully used the LMEA model to investigate an RF discharge thruster and a DC discharge thruster, respectively.

Godyak *et al* [42] measured the discharge electrical characteristics (voltage, current, etc) using argon (99.998% purity) at low pressure inside a glass cylinder with inner diameter of 14.3 (cm), cross-section area = 160 (cm^2), and a discharge gap formed by the two parallel-plate aluminium electrodes of 6.7 (cm). The discharge separation was chosen to be large enough that 'collisionless' discharges at pressures as low as 3.0 (mTorr) could be studied without overlapping electrode sheaths, and small enough that it could be considered as a 1D discharge. For the cases shown, the pressure was 1.0 (Torr) and temperature of 300 K was assumed. The computational grid for all cases tested was composed of 671 nodes equally spaced.

Table 2. Microchannel dimensions and properties of fluid for subsonic gas flows.

Fluid	L (μm)	W (μm)	H (μm)	$P_{\text{in}}/P_{\text{out}}$	P_{out} (kPa)	T_{in} (K)	T_{w} (K)	μ (N s m^{-2})	κ ($\text{W m}^{-1} \text{K}^{-1}$)	k	R ($\text{J kg}^{-1} \text{K}^{-1}$)
N_2	3000	40	1.2	2.701	100.8	314	314	1.85×10^{-5}	0.0259	1.4	296.7

Table 3. Grid dependence test done by Chen *et al* [39] of the centreline u -velocity (m s^{-1}) at different x -locations.

Grid	$x = 500$ (μm)	$x = 1000$ (μm)	$x = 1500$ (μm)	$x = 2000$ (μm)	$x = 2500$ (μm)
1500×7	0.4765853	0.5225323	0.5845432	0.6745498	0.8216915
3000×13	0.4760927	0.5222115	0.5845377	0.6749501	0.8229470
6000×23	0.4759963	0.5222144	0.5845423	0.6749584	0.8229740

Table 4. Grid dependence test done using MIG of the centreline u -velocity (m s^{-1}) at different x -locations.

Grid	$x = 500$ (μm)	$x = 1000$ (μm)	$x = 1500$ (μm)	$x = 2000$ (μm)	$x = 2500$ (μm)
1500×7	0.47601	0.52127	0.58127	0.66794	0.80982
3000×13	0.47606	0.52127	0.58126	0.66798	0.80984
6000×23	0.47620	0.52111	0.58124	0.66794	0.80988

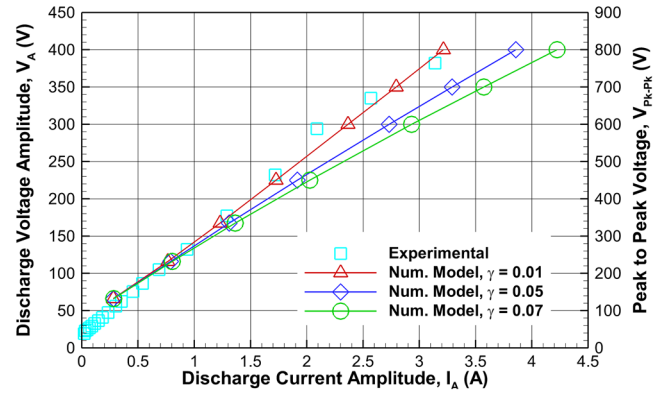
The secondary electron emission (γ) depends sensitively on surface conditions, morphology, impurities, and contamination; the commonly assumed value for (γ) for pure aluminium in a DC discharge is 0.1 [43]. Since in Godyak *et al* [42], the purity of the aluminium or its surface condition are not given and the discharge is not DC, several values of (γ) were tested to validate the code.

The discharge voltage amplitude is applied to each electrode with equal magnitude but opposite phase. The peak-to-peak voltage is the total voltage of the simulation at peak value. Figure 3 shows the comparison between the experimental values and three different numerical simulations performed with different (γ). The cases with (γ) equal to 0.01 matched the experimental results with the least error.

A linear interpolation was used to interpolate between the experimental data points and to calculate the voltage amplitude at the given current amplitude obtained from the numerical model. The maximum percent error of the voltage amplitude in the range of interest for the peak-to-peak voltage (300–800 V) is 5.53% for (γ) equal to 0.01, a reasonable error by drift-diffusion model standards. Drift-diffusion models typically have relatively large errors due to inaccuracies in the input coefficients as well as the model's inherent approximation of the Boltzmann equation. For example, the variation in the reduced mobility (μn_n) when using different collision cross-section libraries, in a Boltzmann solver such as Bolsig+, for the electron mean energy (7–10 eV) region is of $\sim 5\%$ [44].

3.3. CGT and constant thermal heating source thrusters results and comparison

In order to understand the effect of gas heating in the RGEJ, results for adiabatic wall condition cases with different constant thermal heating source values (Q) were obtained and compared with a CGT of the same design. The CGT simulation is called the *base case*. Figure 4 shows the four regions where Q is applied.

**Figure 3.** Comparison between experiment and numerical model.

The performance parameters shown in this study are calculated at the exit plane of the thruster as

$$\begin{aligned} \dot{m} &= 2 \int_0^{H/2} (\rho u) W dy, \\ F_{\text{Thrust}} &= 2 \int_0^{H/2} (\rho u^2 + P) W dy, \\ I_{\text{sp}} &= \frac{F_{\text{Thrust}}}{\dot{m} g_0}, \text{ where } g_0 = 9.81 \text{ (m s}^{-2}\text{)} \text{ and } W = 1 \text{ (cm)}, \\ F_{\tau_{\text{wall}}} &= 2 \int_0^L (\tau_{\text{wall}}) W dx, \text{ where } \tau_{\text{wall}} = \mu \left. \frac{\partial u}{\partial y} \right|_{y=-H/2}. \end{aligned} \quad (12)$$

All other parameters are either defined in literature or previously defined. The following table shows the performance parameters of the different cases studied.

Adding thermal energy to the gas increases the I_{sp} for all cases. A decrease in the mass flow rate requirement occurs for all cases as Q is increased. In the cases where the thermal heating source is applied away from the exit plane, with regions of applied Q labelled 1, 2, or 3, the thrust also decreases due to an increase in the overall shear stress at the wall. Only in the cases where the heat source is placed near the exit plane, at region 4, do we see a gradual increase in thrust with increasing Q .

When the heat source is located near the exit plane, in region 4, we observe a linear decrease of mass flow rate

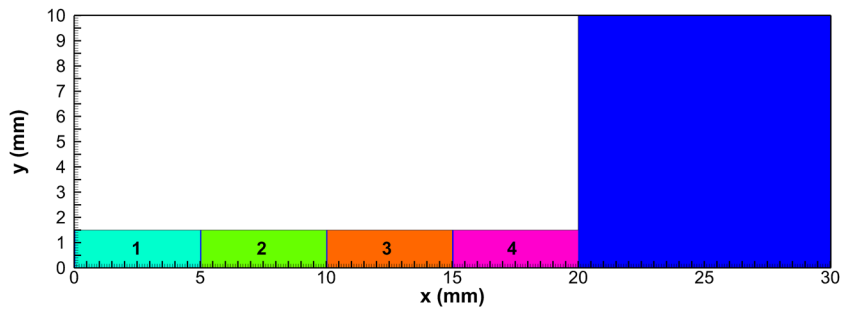


Figure 4. Only half of the domain is shown. Four regions in the domain where Q is applied are shown and labelled 1–4. The value of Q is evenly distributed in each of these regions.

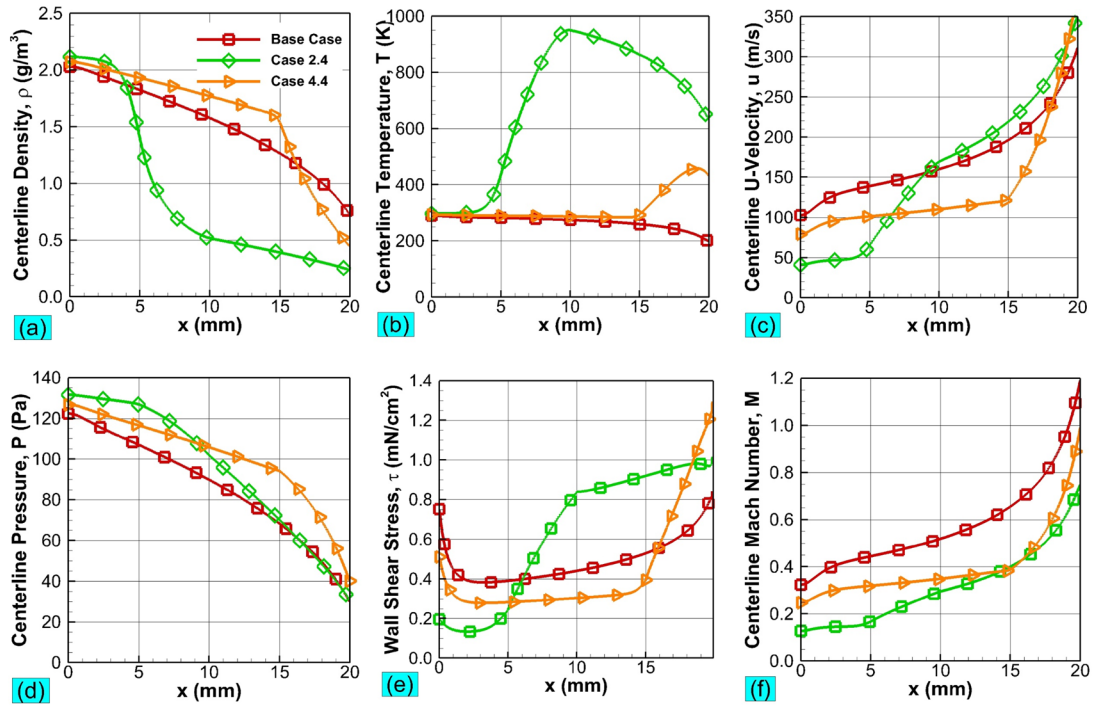


Figure 5. Comparison of *base case*, *case Q2-600*, and *case Q4-600* of (a) density, (b) temperature, (c) tangential velocity, and (d) pressure at the centreline, (e) shear stress at the wall, and (h) Mach number at the centreline. *Cases Q2-600 and Q4-600* have a thermal heating source with a constant value of 4×10^6 (W m^{-3}) distributed over region 2 and 4, respectively.

requirement with a negative slope of 68.6 (SCCM W^{-1}) and a near linear increase in thrust with positive slope of 0.37 (mN W^{-1}), due to an inversely proportional decrease in the shear force at the wall. When the heat source is located closer to the inlet, in region 2, we observe a decrease in the mass flow rate requirement with a slope of 179.7 (SCCM W^{-1}), and a decrease in thrust with a slope of 1.19 (mN W^{-1}). The I_{sp} for all cases increases linearly while Q is less than or equal to 300 (mW), independently of the location where Q is applied. For greater values of Q , with Q applied in regions 1 and 2, the I_{sp} increases with a quadratic trend and the thruster is no longer choked ($M < 1$), for all other cases the linear positive trend is maintained. For the cases with Q equal to 600 (mW), the I_{sp} increases the closer Q is applied to the inlet, with the exception of *case Q1-600* due to the interaction between the applied Q and the inlet boundary condition. *Case Q1-600* characteristics is most likely due to numerical effects.

The following figure shows a comparison between the *base case*, *case Q2-600*, and *case Q4-600*.

If the *thermal creep* term is neglected in the slip flow boundary condition (for simplicity of the analysis), the shear stress is proportional to ρ , u , and $T^{0.5}$ at the wall. Since the mass flow rate requirement is smaller for cases with added thermal energy than for the *base case*, the mass flux (ρu) is smaller in most of the domain along the wall for cases with added Q . Alternatively, the shear stress increases with temperature. These two competing contributions, (ρu) and (s), cause the shear stress to decrease before the region where Q is added and increase right after. The *thermal creep* plays a minor role that increases this effect since molecules creep from cold towards hot regions [45]. The *thermal creep* contribution to the shear stress is negative while T is increasing and positive while T is decreasing along the tangential direction at the wall. The shear force in *case Q2-600* at the wall increased by about $\sim 30\%$ when compared to the *base case*. For *case Q4-600*, the shear force is $\sim 10\%$ lower than the *base case*. For both cases, the shear force causes an inversely proportional change in the thrust of similar percentage. The total shear force experienced

by the fluid and the thrust produced by the device depends on the fraction of the wall area that is exposed to the higher temperatures. This observation shows that if maximizing the thrust in the device was the most desirable objective, the Q should be applied closer to the exit plane to minimize viscous losses.

For case $Q2-600$, the most drastic change in comparison to the *base case* due to the addition of thermal energy in figure 5 occurs in (a) density and (b) temperature. At the exit plane, (T) increases by a factor of (~ 3) and (ρ) decreases inversely proportional. The increase in (s) at the exit plane, as observed in figure 5(b), increases the speed of sound. The Mach number at the exit plane, figure 5(f), decreases from 1.0 for the *base case* to 0.75 for case $Q2-600$, despite (u) increasing by 13%. The addition of thermal energy has caused the flow to change from choked flow ($M_{\text{Throat}} \sim 1$) to subsonic ($M_{\text{Throat}} < 1$), meaning that viscous losses play an important role in this particular pressure regime for this channel design and prevent the exit tangential velocity from increasing with ($T^{0.5}$) in a directly proportional manner. The pressure profile, figure 5(d), has a gradual slope until heat is added at ($x = 6$ mm) and decreases with a steeper slope from this point on. Exit plane (P) is virtually unaffected, only 4% higher. At the exit plane, (P) and (u) change only a small amount in comparison to (ρ) for case $Q2-600$. Given that $\dot{m} \sim (\rho_e u_e)$, $F_{\text{Thrust}} \sim (\rho_e u_e^2 + P_e)$ and $I_{\text{sp}} \sim u_e + P_e/\dot{m}$, the mass flow rate and thrust decrease as (ρ) decreases while the I_{sp} increases due to the (P_e/\dot{m}) term increase, since $P_e/\dot{m} \propto 1/\rho_e \propto T_e$ if P_e remains unchanged when compared to the *base case*.

For case $Q4-600$, at the exit plane (T) increases by a factor of (~ 2), (ρ) decreases by 40%, (P) and (u) increase by 33% and 23%, respectively, in comparison to the *base case*. Although the increase in (P) and (u) are beneficial to increase the I_{sp} , the I_{sp} percent increase for this case is not as significant as for case $Q2-600$. The decrease in (ρ) at the exit plane plays the most important role in increasing the I_{sp} and it is inversely proportional to the increase in (T).

The *base case* has an exit Reynolds number of ~ 33 , proving our initial assumption that an expansion nozzle would be counterproductive to increase the specific impulse since ($\text{Re} < 100$). All other cases have smaller exit Reynolds number due to heat addition. Increasing the tangential momentum accommodation coefficient in the slip flow boundary conditions from 0.89 to 1.0 increased the I_{sp} for case $Q2-450$ by 4%. The *thermal creep* (transpiration) effects can affect the variation of pressure caused by tangential temperature gradients [45]. The *thermal creep* was only significant for cases with very high temperatures (~ 900 K), such as case $Q2-600$, where the shear stress changes by ~ 2 (N m^{-2}) (20% the max. value) in the region between ($5 \text{ mm} < x < 10 \text{ mm}$) due to the *thermal creep*. The higher-order slip flow boundary condition presented by Xue *et al* [46] were tested for cases with low temperature, e.g. $Q2-450$, and compared with cases using equation (9) and no effect in the I_{sp} was detected.

The Kn at the centreline for the *base case* is 1.9×10^{-2} at the inlet and 4.5×10^{-2} at the exit plane, while for case $Q2-600$ the Kn is 1.8×10^{-2} at the inlet, and as high as 2.0

$\times 10^{-1}$ at the exit plane. The Kn_{Exit} for case $Q2-600$ is the highest of all cases and higher than the recommended range of values for slip flow regime ($0.001 < \text{Kn} < 0.1$). Maurer *et al* [47] estimated the upper limit of the slip flow regime as $\text{Kn} = 0.3 \pm 0.1$ [45], where Kn is based on the channel height as in their study. For RGEJ, only the cases with ($\text{Kn} < 0.1$ or $\text{Kn} \sim 0.1$) will be presented and studied.

Based on this study, region 2 was picked as the best location to apply the thermal heating source in order to increase the I_{sp} . The closer Q is applied to the inlet, the higher the exit (T), see case $Q2-600$ versus case $Q4-600$ in figure 5(b), which proportionally relates to the I_{sp} . Region 1 was not picked due to its interaction with the inlet boundary condition. The decrease in thrust experience by the cases with Q applied in region 2 could be counteracted by using a greater number of slots or a wider slot in the device if a given thrust is necessary.

3.4. RGEJ thruster performance

The following table shows the performance parameters of several cases with plasma-aided technology at different voltages with geometry, mesh, and boundary conditions as defined in figure 2.

In general, the plots of \dot{m} , F_{Thrust} , F_{Wall} , and I_{sp} as functions of Q follow similar trends as the previous cases with constant thermal heating source applied in region 2. The current, thermal heating source and power versus voltage are discussed in the subsequent section. The thrust effectiveness was calculated by adjusting the width of the device for each case to match the mass flow rate of the *base case*, subtracting the thrust of the *base case* from the adjusted thrust of each case and dividing this difference by the power consumption (P_{W}). The effectiveness of the device increases linearly with increasing voltage with a slope of 1.8 ($\text{mN W}^{-1} \text{V}^{-1}$). The highest effectiveness is obtained for case 750 V with an effectiveness of 2.106 (N W^{-1}), by comparison, the MPT has an effectiveness of 50 ($\mu\text{N W}^{-1}$) for the 750 (V) and 650 (mW) case with I_{sp} of 74 (s) [5, 8].

In table 5, the Q versus I_{sp} have positive slopes, 31.5 (s W^{-1}), approximately linear for the range of Q between 0–300 (mW) and independent of the location where Q is applied. The plasma-aided cases of RGEJ, shown in table 6, have a significantly higher Q versus I_{sp} positive slope, 54.8 (s W^{-1}), which indicates that concentrating the total value of Q in a smaller region of the domain is beneficial to increase the I_{sp} for adiabatic cases. Case 750 V has an I_{sp} of 60.7 (s), a 37.6% improvement over the *base case*. The I_{sp} of RGEJ, (60.7s), operating at 750 (V) is 16% higher than the I_{sp} of a highly optimized argon propellant CGT, (52s), and 35% higher than the I_{sp} of the argon propellant FMMR, (45s) [1]. The increase in I_{sp} for case 750 V over CGTs is achieved with only 406 (mW) per centimetre of width of the device and 98.5% of the total electrical power is converted to heating of the neutral gas, which is higher than the range (81–95%) predicted by Houba and Roy [17] for a device operating at assumed constant temperature (300 K) and pressure (0.6 Torr) using air as the working fluid. The remainder of the discharge power goes into the electrons, which lose energy in inelastic

Table 5. Values of total thermal heating source (Q), mass flow rate (\dot{m}), thrust (F_{Thrust}), shear force ($F_{\tau_{\text{wall}}}$), specific impulse (I_{sp}), specific impulse increase ($I_{\text{sp Inc.}}$) compared to the *base case*, exit plane Mach number (M_{Exit}) at the centreline, and exit Knudsen number (Kn_{Exit}) at the centreline are displayed. Q , \dot{m} , F_{Thrust} , and $F_{\tau_{\text{wall}}}$ are per centimetre of width ($W = 1 \text{ cm}$) of the device. For mass flow rate, SCCM means cubic centimetre per minute at STP.^a

Case	Region of applied Q as shown in figure 4	Q (mW)	\dot{m} (SCCM)	F_{Thrust} (mN)	$F_{\tau_{\text{wall}}}$ (mN)	I_{sp} (s)	$I_{\text{sp Inc.}}$ (%)	M_{Exit} —	Kn_{Exit} —
<i>Base case</i>	None	0	178.0	2.288	1.955	44.11	—	1.192	0.046
<i>Case Q1-150</i>	1	150	147.9	2.069	2.112	48.00	8.82	1.138	0.063
<i>Case Q1-300</i>	1	300	118.7	1.841	2.298	53.21	20.64	1.056	0.089
<i>Case Q1-450</i>	1	450	89.8	1.600	2.516	61.15	38.65	0.924	0.133
<i>Case Q1-600</i>	1	600	61.3	1.370	2.746	76.65	73.79	0.722	0.208
<i>Case Q2-150</i>	2	150	152.6	2.145	2.046	48.24	9.38	1.143	0.061
<i>Case Q2-300</i>	2	300	127.7	1.991	2.167	53.50	21.29	1.074	0.085
<i>Case Q2-450</i>	2	450	102.3	1.816	2.323	60.89	38.05	0.969	0.121
<i>Case Q2-600</i>	2	600	68.3	1.563	2.566	78.45	77.87	0.750	0.203
<i>Case Q3-150</i>	3	150	159.5	2.243	1.966	48.28	9.45	1.152	0.059
<i>Case Q3-300</i>	3	300	141.6	2.189	1.998	53.06	20.30	1.102	0.077
<i>Case Q3-450</i>	3	450	124.1	2.125	2.050	58.74	33.18	1.039	0.100
<i>Case Q3-600</i>	3	600	106.4	2.047	2.124	66.03	49.71	0.954	0.131
<i>Case Q4-150</i>	4	150	167.3	2.360	1.885	48.41	9.76	1.119	0.056
<i>Case Q4-300</i>	4	300	156.9	2.421	1.830	52.96	20.06	1.071	0.068
<i>Case Q4-450</i>	4	450	146.7	2.472	1.789	57.80	31.05	1.030	0.082
<i>Case Q4-600</i>	4	600	136.7	2.512	1.756	63.04	42.93	0.991	0.098

^a The values shown were obtained using adiabatic conditions, not taking into account the heat loss through the walls due to conduction and radiation.

collisions due to the various ionization, attachment, and excitation reactions [17].

The following figures show a comparison of the results of the rarefied gas simulations.

Figure 6(c) shows how the plasma electro-thermal heating source locally heats the gas in *case 750 V* to temperatures as high as ($\sim 640 \text{ K}$) near the corner of the cathode electrode where high electric field causes the heating source to increase sharply. By comparison, the *base case* has a temperature profile that decreases along the x -axis direction as we approach the exit plane due to the flow expansion. In figure 6(g), the exit temperature at the centreline is higher for higher voltage cases with *case 750 V* having a temperature of ($\sim 400 \text{ K}$), twice the value of the *base case* ($\sim 200 \text{ K}$). The speed of sound doubles for *case 750 V*.

The pressure profile, see figures 6(d) and (h), is affected by the addition of thermal energy to the flow. The *base case* shows a near linear decrease in pressure for ($x < 11 \text{ mm}$) with ($-\partial P/\partial x$) $\sim 3.5 \text{ (Pa mm}^{-1}\text{)}$, followed by a parabolic decrease. Four important effects are encountered in micro-flows: *rarefaction*, *compressibility*, *viscous heating*, and *thermal creep* [45]. Out of those, *compressibility* and *rarefaction* are competing effects. The curvature in the pressure distribution in compressible flows is due to *compressibility* effects, the higher the Mach number the greater this effect becomes, the curvature increases with increased inlet to outlet pressure ratios [45]. *Rarefaction* decreases the curvature in the pressure distribution, which becomes increasingly linear as the free-molecular flow regime is approached with increasing Kn numbers [45]. In the pressure profile in figure 6(h), *rarefaction* is dominant in the *base case* for ($x < 11 \text{ mm}$) and the *compressibility* effects become increasingly important in the rest of the domain due to increasing Mach number. For all the plasma-aided cases,

case 450 V–750 V, the pressure profile is very similar independent of voltage (thermal energy input), but the pressure profile has two distinct linear regions, one before and one after the area where thermal energy is deposited. The effect of *rarefaction* dominates for ($x < 16 \text{ mm}$) due to the higher Kn numbers found in the plasma-aided cases in comparison to the *base case*. For *case 750 V*, the two distinct linear regions have ($-\partial P/\partial x$) $\sim 1.5 \text{ (Pa mm}^{-1}\text{)}$ for ($x < 7 \text{ mm}$) and $5.5 \text{ (Pa mm}^{-1}\text{)}$ for ($7 \text{ mm} < x < 16 \text{ mm}$), respectively. These two different regions are caused by the difference in temperature which affects the shear stress at the wall in the same manner as the cases in table 5.

The tangential velocity plots, in figure 6(b), show the effect of having two distinct ($-\partial P/\partial x$) regions in *case 750 V*. The *base case* has a constant acceleration of the flow along the channel, but *case 750 V* has approximately constant velocity before thermal energy is added due to the low ($-\partial P/\partial x$) for ($x < 7 \text{ mm}$) follow by an acceleration region where ($-\partial P/\partial x$) is higher. The acceleration region is similar to a shorter channel operating with the same inlet to outlet pressure ratio at a higher inlet temperature. This observation may be useful to modify the geometry of the thruster's design in the future for optimization purposes.

The addition of thermal energy increases the tangential velocity at the exit plane centreline from $311 \text{ (m s}^{-1}\text{)}$ in the *base case* to $362 \text{ (m s}^{-1}\text{)}$ in *case 750 V* and decreases the density from $0.73 \text{ (mg m}^{-3}\text{)}$ to $0.36 \text{ (mg m}^{-3}\text{)}$, increasing the I_{sp} of the thruster. Due to low Reynolds numbers (< 30) in all cases and dominant viscous terms, no shock discontinuities are found. As the Reynolds number decreases with increasing temperature (thermal energy input), the viscous losses increase causing a degradation of the thrust, which could be counteracted by extending the width of the device.

Table 6. Values of: voltage (V), mass flow rate (\dot{m}), thrust (F_{Thrust}), shear force ($F_{\tau_{\text{Wall}}}$), specific impulse (I_{sp}), specific impulse percent increase ($I_{\text{sp Inc.}}$), current (I), total thermal heating source (Q), total electrical power (P_{W}), fraction of the total electrical power converted into thermal heating source (Q/P_{W}), and effectiveness of the thrust (ζ_{Thrust}) at the same mass flow rate as the *base case*. (\dot{m}), (s_{Thrust}), ($F_{\tau_{\text{Wall}}}$), (I), (Q), and (s_{W}) are per centimetre of width ($i = 1$ cm) of the device.^a

Case	V (V)	\dot{m} (SCCM)	F_{Thrust} (mN)	$F_{\tau_{\text{Wall}}}$ (mN)	I_{sp} (s)	$I_{\text{sp Inc.}}$ (%)	I (mA)	Q (mW)	s_{W} (mW)	s/P_{W} (%)	ζ_{Thrust} (N W^{-1})
<i>Base case</i>	0	178.0	2.288	1.955	44.1	—	0.000	0	0	—	—
<i>Case 450 V</i>	450	134.7	2.039	2.113	51.9	17.7	0.538	240	242	99.4	1.557
<i>Case 550 V</i>	550	122.1	1.964	2.187	55.2	25.1	0.570	308	313	98.3	1.770
<i>Case 650 V</i>	650	112.1	1.898	2.253	58.1	31.7	0.565	360	367	98.0	1.963
<i>Case 750 V</i>	750	104.2	1.843	2.308	60.7	37.6	0.541	400	406	98.5	2.106

^a The values shown were obtained using adiabatic conditions, not taking into account the heat loss through the walls due to conduction and radiation.

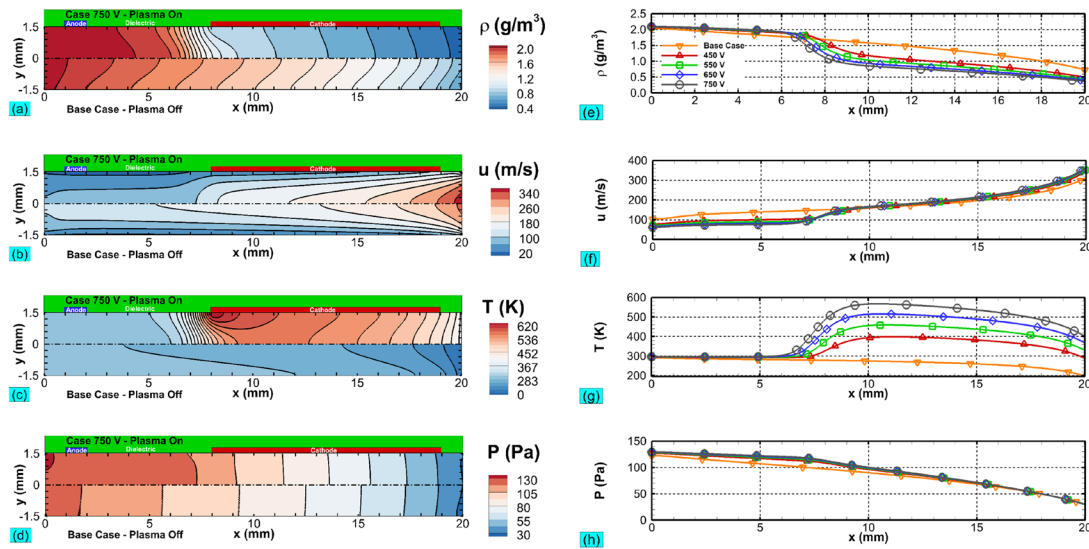


Figure 6. (a)–(d) Comparison of rarefied gas results between the *base case* on the bottom half and *case 750 V* on the top half, and (e)–(h) comparison of rarefied gas centreline results for the *base case* and all plasma cases. Variables compared are ((a) and (e)) density (ρ), (b) and (f) tangential velocity (u), (c) and (g) temperature (T), and ((d) and (h)) pressure (P).

The *thermal creep*, a *rarefaction* effect, plays a significant role close to the cathode electrode corner at (~ 8 mm) where the magnitude of ($\partial T/\partial x$) is the highest, causing a sharp discontinuity in the profile of shear stress at the wall. In this location, the shear stress abruptly increases due to the *thermal creep*, but the *thermal creep* effect is negligible in the rest of the domain. In the cases presented, the *viscous heating* effect is not apparent since for pressure-driven compressible flows the expansion cooling negates it [45].

The following figures show a comparison of the results of the ionized gas simulations for the given DC voltages. The applied voltage was varied from 450 to 750 (V), this range is within the operating conditions of the validation cases.

Figures 7(a)–(c) and (g)–(i) display a comparison of the contours for the electrons number density, positive ions number density, and electron energy density with their higher values right before the cathode fall region. For *case 750 V* the maximum values reach 4.03×10^{16} (m^{-3}), 4.23×10^{16} (m^{-3}), and 0.045 (J m^{-3}), respectively. The metastable atoms number densities, not shown, are approximately two orders of magnitude lower than the charged particles and their contribution to ionization is very small for the given pressure operation regime. The electron temperature (T_e), calculated using

the electron energy and number densities, is (~ 4 eV) in the plasma column for all cases. In the cathode fall, where electron number density decreases to very small values ($< 10^{13}$ m^{-3}) by comparison to the peak value ($\sim 10^{16}$ m^{-3}), the (T_e) is over-predicted and can increase exponentially in this region of vanishing electron densities due to a numerical artefact of the fluid model [5]. This behaviour of (T_e) does not affect the accuracy of the simulations for the other variables since the electron energy content is negligible in this part of the domain [5]. Figures 7(f) and (l) show the thermal heating source, concentrated in the cathode fall, reaching a maximum value of 4×10^8 (W m^{-3}) near the corner of the cathode for *case 750 V*. Although this value looks large, it is concentrated in a small region of the domain and the net value of the thermal heating source is orders of (~ 100 s mW).

An interesting finding in this comparison of cases at different voltages is that the cathode fall region is increased with increasing voltage while compressing the region of the plasma column. When *case 450 V* and *case 750 V* are compared in figures 7(a)–(f), we can observe a shift towards the inlet of the charged particle number densities and electric potential peaks. The peak values of the number densities of charged particles remain relatively constant, $\sim 4 \times 10^{16}$ (m^{-3}) for cases

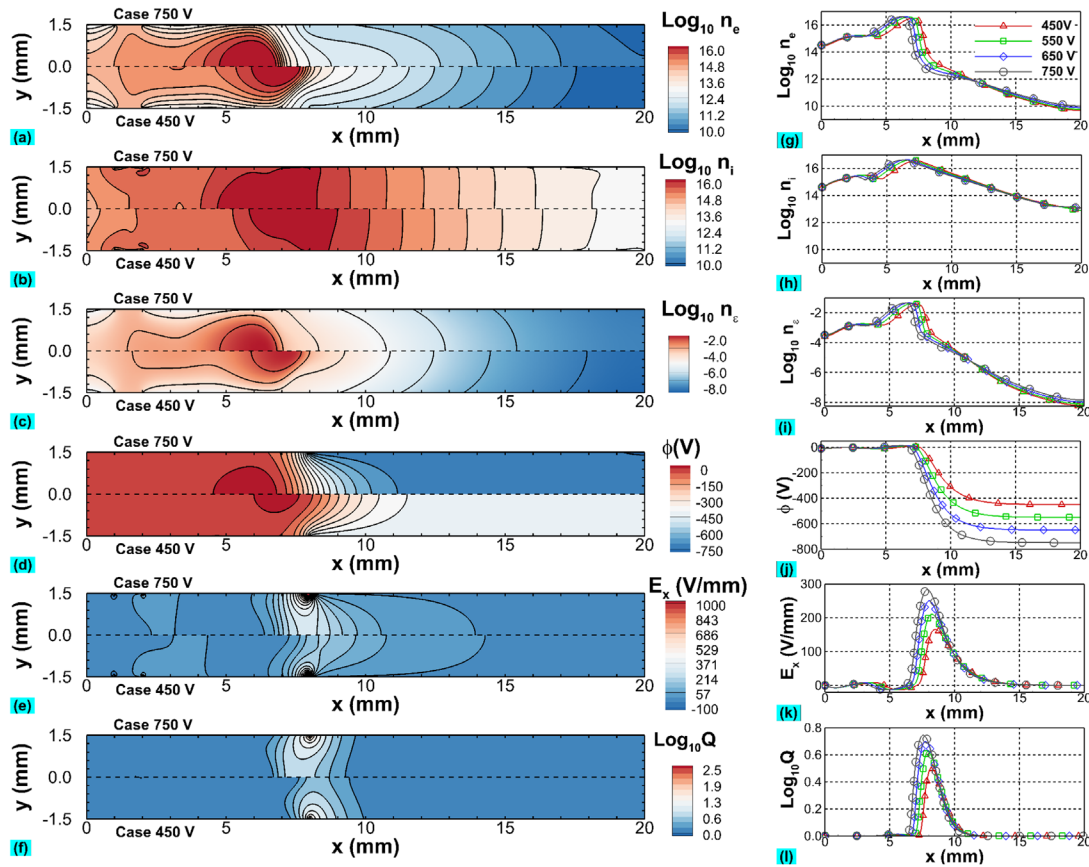


Figure 7. (a)–(f) Comparison of plasma discharge results for *case 450 V* and *case 750 V*, and (g)–(l) comparison of plasma-discharge centreline results for all cases. (a), (g) Electron number density (m^{-3}), (b) and (h) ion number density (m^{-3}), (c) and (i) electron energy density (J m^{-3}), (d) and (j) electric potential (V), (e) and (k) electric field tangential component (V mm^{-1}), and (f) and (l) electro-thermal heating source (W cm^{-3}).

with 550–750 (V), as the voltage is increased. The peak value for *case 450 V* is $\sim 3 \times 10^{16} \text{ (m}^{-3}\text{)}$. For constant gas pressure and temperature cases, the number density of charged particles would drastically increase with increasing voltage, for a pressure-driven compressible flow in a channel the discharge seems to be self-limiting for the given operational parameters. This phenomenon is related to the decrease in number density of neutrals as the gas temperature increases, both due to the localized heating. In the ion flux (Γ_i), the main contributor of current at the cathode, the ion mobility increases with increasing voltage due to an increase in electric field and a decrease in neutral number density which increases the reduced electric field ($|\mathbf{E}|/n$). The ion diffusion, as established in the Einstein relation ($D_i = k_b T_i \mu_i / e$), is further increased by the increase in ion temperature which is assumed to be the temperature of the gas due to rapid thermalization of the ions with other heavy particles. Since the ion diffusion is more sensitive to the effects of thermal energy addition to the gas than the mobility, the diffusion term of the ion flux causes the ion number density to decrease close to the cathode as voltage and thermal heating increase.

Most of the ionization happens close to edge of the plasma column before reaching the cathode fall and it is concentrated around the centreline, similar to the RFET when it is working at low pressures (1.5 Torr) [9]. The ions flow from this region of high electric potential, but low electric field, to the walls

where they recombined. In contrast, the electrons flow from the cathode to the rest of the walls, most of them flow into the anode and the rest into the dielectric sections of the walls to balance the ion current. The number of ions leaving the thruster through the exit plane is negligible; therefore their contribution to the thrust is neglected. Some power is always lost through inelastic collisions to solid walls and the outflow, but the heating of the walls due to neutralization is not taken into account since our assumption of adiabatic walls is just an approximation to simplify the numerical simulation of a well-insulated thruster.

3.5. RGEJ thruster discharge characteristics

The performance plasma-discharge characteristics of RGEJ are presented in this section. The discharge current is obtained by integrating the species current over the length of the electrode [17]

$$I = 2e \int_{L_{\text{Electrode}}} \left(\sum_k \Gamma_k \cdot \hat{n} \right) W dx. \quad (13)$$

The total electrical power (P_W), shown in table 6 is calculated from the relation $P_W = VI$. The net tangential plasma induced electrostatic force and the net thermal heating source are obtained by integrating equations (4) and (5) over the channel volume

heat loss through conduction of the internal walls at $T = f(x)$ is 36.6 (mW) per centimetre of width of the thruster. For a well-insulated satellite, a MEMS thruster system external average temperature is 285 K [48]. At this new T_{surr} , leaving a small gap in the right hand side of the domain between the thruster insulation layer and the wall of the microsatellite at $T = f(y)$, with an additional aluminium foil layer, the RGEJ heat loss through conduction would decrease to 7.4 (mW) per centimetre of width of the thruster. A further reduction of heat loss via conduction could be achieved by stacking many thruster's slots next to each other, similarly to FMMR.

In figure 9(b), the radiation analysis was performed using 400 plates in each internal wall, assuming each is a diffuse-grey surface. The inlet plane is considered a diffuse-grey surface with the emissivity of tungsten since the plenum chamber will contain micro-machined pillars or a porous metal material to heat the propellant. The background radiation temperature of outer space is assumed to be 0.0 K. The emissivities of the dielectric and electrodes were assumed to be 0.85 (boron nitrate) and 0.04 (tungsten), respectively. The heat loss due to radiation is 48.6 (mW). If materials with lower emissivities are used, such as aluminium oxide on fused silica ($\epsilon_{\text{Al}_2\text{O}_3} = 0.24$) and aluminium ($\epsilon_{\text{Al}} = 0.02$) [49], the radiation heat loss decreases to 30.1 (mW). The radiation heat loss depends strongly on the emissivity of the internal walls.

The adiabatic assumption in the cases presented is intended to provide an upper limit for the thruster's performance for the given operational parameters. The overall heat losses of a thruster working in outer space would be 37.5–85.26 (mW), which is 9–21% of the input power in *Case 750 V*, depending on the internal temperature of the micro-satellite, the insulation layer of the thruster, and the emissivity of the internal walls. In laboratory conditions, with an environment temperature of 300 K, the heat loss through conduction would be negligible in a well-insulated thruster and the heat loss through radiation would be 23.9 (mW), which is 5.9% of the input power, making the assumption of adiabatic walls a reasonable approximation for a comparisons with experiments.

4. Conclusion

The RGEJ device shows encouraging results with an improvement in I_{sp} of 37.6% over CGTs with the same geometry and working parameters, an improvement in I_{sp} of 16% over optimized argon propellant CGTs, and an improvement in I_{sp} of 35% over argon propellant FMMR. Based on the I_{sp} versus voltage characteristics, the thruster could operate at an even higher voltage to further increase the I_{sp} . For the configuration of electrodes studied and range of voltages, the majority of the energy is converted into gas heating (~98%); the plasma force plays a negligible role in the injection of momentum. High heat loss is typical in MEMS-scale micro-nozzles [1]. For example, FMMR required twice (200% of) the power use to heat the gas to operate due to heat losses. In contrast, a simple thermal analysis estimated that the proposed RGEJ thruster would require between 9% to 21% more input power

to maintain the same performance due to heat loss in outer space, this number could be decreased by reducing heat loss through conduction and radiation by stacking many thruster's slots and using a dielectric material with lower emissivity.

Loosely coupling the finite element based rarefied gas module and the finite difference based IGM in the MIG framework resulted in a stable approach to solve internal, slip flow problems with glow discharges. These type of problems are highly unstable since the plasma and gas interact strongly with each other, but their time scales are widely different by $O(10^{-5})$ s. The approach used in this study circumnavigates this problem by increasing the voltage in small increments and by having several conversion criteria as explained in the introduction of section 2. Using finite difference to solve the ionized gas is faster than using finite volume for rectangular geometries. While using the finite element based rarefied gas module will allow the analysis of more complex geometries in the future.

Argon was selected as the working fluid because it is the noble gas of choice for benchmarking plasma numerical codes due to the few reactions necessary to model the glow discharge at low pressure. However, thermal thruster developers prefer to use gases with lower molecular weight and higher gas constant. Our goal is to eventually develop a phase-change thruster concept that uses liquid or solid propellant, instead of argon, to avoid heavy storage tank and valve leakage problems, vaporizing the propellant on demand to generate thrust. The low minimum required operating pressure (1 Torr) is selected by design to eventually develop this class of thruster. In future simulations, a different gas with better-suited properties for the RGEJ thruster should be used and the geometry of the thruster should be optimized. Future simulations will focus on the effect of varying the operational parameters.

Acknowledgments

This work was supported by the Space Research Initiative (SRI) program, a joint program between the NASA Kennedy Space Center, University of Central Florida and the University of Florida. The authors would like to thank all members of the SRI project that collaborated to its success and both universities for their support.

ORCID iDs

Subrata Roy  <https://orcid.org/0000-0002-2316-0854>

References

- [1] Patric Micci M M and Ketsdever A D 2000 *Micropropulsion For Small Spacecraft (Progress in Astronautics and Aeronautics vol 187)* (Reston, VA: AIAA) (<https://doi.org/10.2514/4.866586>)
- [2] Ketsdever A *et al* 2000 Fabrication and testing of the free molecule micro-reistojet: initial results *36th AIAA/ASME/SAE/ASEE Joint Propulsion Conf. and Exhibit (Huntsville, AL)* (<https://doi.org/10.2514/6.2000-3672>)

- [3] Soni J 2014 Characterization of plasma actuator based microthruster concepts for high altitude aircrafts and cubsats *PhD Thesis* Department of Aerospace and Mechanical Engineering, University of Florida, Gainesville
- [4] Roy S 2016 Method and apparatus of small satellite propulsion *US Patent No.* 9228570
- [5] Deconinck T 2008 Simulation studies of direct-current microdischarges for electric propulsion *PhD Thesis* Department of Aerospace Engineering and Engineering Mechanics, The University of Texas, Austin, TX
- [6] Greig A *et al* 2015 *Front. Phys.* **2** 1–9
- [7] Takahashi T *et al* 2009 *Phys. Plasmas* **16** 1–14
- [8] Deconinck T *et al* 2009 *J. Appl. Phys.* **106** 063305
- [9] Charles C and Boswell R 2012 *Plasma Sources Sci.* **21** 1–4
- [10] Balagangadhar D and Roy S 2001 *Comput. Methods Appl. Mech. Eng.* **190** 5465–79
- [11] Roy S 2000 *Comput. Methods Appl. Mech. Eng.* **184** 87–98
- [12] Rafatov I 2012 *Phys. Plasmas* **19** 033502
- [13] Boeuf J P and Pitchford L C 1995 *Phys. Rev.* **51** 1376
- [14] Rafatov I *et al* 2012 *Phys. Plasmas* **19** 093503
- [15] Mahadevan S and Raja L L 2010 Simulation of direct-current surface plasma discharges in air for supersonic flow control *AIAA J.* **50** 325–37
- [16] Hagelar G J M and Pitchford L C 2005 *Plasma Sources Sci. Technol.* **14** 722–33
- [17] Houba T and Roy S 2015 *J. Appl. Phys.* **118** 1–9
- [18] Biagi-v7.1 database www.lxcat.net (Accessed: 30 January 2015)
- [19] Petrov G M and Ferreira C M 1998 *Phys. Rev. E* **59** 3571–82
- [20] Rafatov I *et al* 2007 *Phys. Lett. A* **367** 114–9
- [21] Sitaraman H and Raja L L 2012 *J. Phys. D: Appl. Phys.* **45** 1–11
- [22] Boeuf J P *et al* 2005 *Appl. Phys. Lett.* **86** 1–3
- [23] Phelps A V and Petrovic A L 1999 *Plasma Sources Sci. Technol.* **8** R21–44
- [24] Scharfetter D and Gummel H 1969 *IEEE Trans. Electron Devices* **16** 64–77
- [25] Raju R 2003 Hydrodynamic model for investigation of gas flows through micro-geometries and nanopores *MS Thesis* Mechanical Engineer Department, Kettering University, Flint, MI
- [26] Hanley H 1973 *J. Phys. Chem. Ref. Data* **2** 619–42
- [27] Goldston R J and Rutherford P H 1995 *Introduction to Plasma Physics* (Bristol: CRC Press)
- [28] Choudhuri A R 1998 *The Physics of Fluids and Plasmas: an Introduction for Astrophysicists* (Cambridge: Cambridge University Press) (<https://doi.org/10.1017/CBO9781139171069>)
- [29] Maxwell J C 1879 *Phil. Trans. R. Soc. A* **170** 231–56
- [30] Smoluchowski V M 1898 *Ann. Phys. Chem.* **64** 101–30
- [31] Agrawal A and Prabhu S V 2008 *J. Vac. Sci. Technol. A* **26** 634–45
- [32] Trott W M *et al* 2007 Experimental measurement of thermal accommodation coefficients for microscale gas-phase heat transfer *AIAA Paper 2007-4039* (<https://doi.org/10.2514/6.2007-4039>)
- [33] Donea J and Huerta A 2003 *Finite Element Methods for Flow Problems* (New York: Wiley)
- [34] Roy S and Pandey B P 2003 *J. Propul. Power* **19** 964–71
- [35] Roy S *et al* 2003 *J. Appl. Phys.* **93** 4870–9
- [36] Roy S and Gaintonde D 2006 *Phys. Plasmas* **13** 023503
- [37] Kumar H and Roy S 2005 *Phys. Plasmas* **12** 093508
- [38] Ketsdever A D *et al* 2005 *AIAA J.* **43** 633–41
- [39] Chen C S *et al* 1998 *Numer. Heat Trans. A* **33** 749–62
- [40] Pong K C *et al* 1994 *ASME-Publications-FED* **197** 51
- [41] Houba T 2016 Parallel 3D numerical simulation of dielectric barrier discharge plasma actuators *PhD Thesis* Department of Aerospace and Mechanical Engineering, University of Florida, Gainesville, FL
- [42] Godyak V A *et al* 1991 *IEEE Trans. Plasma Sci.* **19** 660–76
- [43] Lieberman M A and Lichtenberg A J 2005 *Principles of Plasma Discharges and Materials Processing* (Hoboken, NJ: Wiley) (<https://doi.org/10.1002/0471724254>)
- [44] Pancheshnyi S *et al* 2012 *Chem. Phys.* **398** 148–53
- [45] Karniadakis G E *et al* 2006 *Microflows and Nanoflows: Fundamentals and Simulation* vol 29 (New York: Springer) (<https://doi.org/10.1007/0-387-28676-4>)
- [46] Zhang W M *et al* 2012 *Microfluid Nanofluidics* **13** 845–82
- [47] Maurer J *et al* 2003 *Phys. Fluids* **15** 2613–21
- [48] Kang S and Oh H 2016 *Int. J. Aerosp. Eng.* **2016** 1–17
- [49] Henninger J 1984 *Solar Absorptance and Thermal Emittance of Some Common Spacecraft Thermal-Control Coatings* (Washington, DC: NASA) (<http://www.dtic.mil/docs/citations/ADA305864>)